Geochemical Perspectives Letters

Dominant monosulfide solid solution fractionation causes Cu deficit in continental crust

Y.C. Zheng, Q.S. Sun, J. Mu, W.Q. Li, C.D. Wu, S.H. Liu, Y. Zhao

Supplementary Information

The Supplementary Information includes:

- Geological Setting and Samples
- Methods
- Results
- Tables S-1 to S-2
- Figures S-1 to S-6
- Supplementary Information References

Geological Setting and Samples

The Gangdese continental arc recorded a long, punctuated history of magmatism spanning ca. 210 Ma to 50 Ma, with activities peaking at 210–175 Ma and 110–80 Ma (Fig. 1). The arc lower crust represented by the highly metamorphosed (amphibolite– to granulite–facies) Jurassic and Late Cretaceous gabbros and ultramafic–mafic hornblendites were exhumed from depths of 30–50 km to the surface (Zhang *et al.*, 2020). These hornblendites occur as large bodies with hundreds of meters to kilometres in length within the gabbros. Samples used in this study were mostly collected from the newly excavated Sichuan-Tibet railway tunnels that are hundreds of meters from the surface. The hornblendites are interpreted as cumulates formed through fractional crystallisation of the basaltic arc magmas represented by the parental magmas of Milin meta-gabbros (Xu *et al.*, 2019; Zhang *et al.*, 2020). The Milin (93 Ma), Zhaxiraodeng (88 Ma) and Jinba (73 Ma) hornblendites are mainly composed of hornblende (70~80 %) with variable amounts of biotite (5~15 %), and minor amounts of clinopyroxene (less than 5 %), sulfides, magnetite and ilmenite. The Cuijiu (200 Ma) and Sengbo (90 Ma) cumulates exhibit similar mineral assemblages, but have evidently higher contents of magnetite (5~10 %) and plagioclase (5~10 %), while the Sengbo cumulates also contain some garnet (5~10 %) (Fig. S-1).

All the cumulates fall on the second and third segments of the Z-shaped cumulate line determined by experimental studies of hydrous differentiation of basaltic melts under 0.7-1.5 GPa (Müntener and Ulmer, 2018) (Fig. S-2a), with a good correspondence in the plot of MgO *vs* FeO^T (Fig. 2a). Thus, this indicates that rocks from the Milin,

Zhaxiraodeng and Jinba represent the relatively preliminary cumulates produced by dominantly accumulation of clinopyroxene + amphibole, while with decreasing clinopyroxene and amphibole, together with increasing plagioclase ± magnetite, those from Cuijiu and Sengbo counterparts form.

The sulfides are dominated by pyrrhotite, pyrite, chalcopyrite, with minor pentlandite and millerite, and occur in the form of inclusions mainly in hornblende, clinopyroxene, and magnetite, or in the interstices between these minerals (Fig. S-1), indicating a magmatic origin. Under microscope, these sulfides are characterised by a smooth surface without any alteration by secondary sulfides or metal-oxides.

Methods

Cu isotope analysis

Only samples without metasomatism by later silicate melts and hydrothermal fluids, and free of surface weathering were used here. Copper isotope data are reported in standard δ-notation in per mil relative to the standard reference material (SRM) NIST 976:

$$\delta^{65}Cu = [(^{65}Cu / {}^{63}Cu)_{sample} / (^{65}Cu / {}^{63}Cu)_{NIST976} - 1] \times 1000 \qquad \text{(Eq. S-1)}$$

Whole-rock copper isotope compositions were measured at the Isotope Geochemistry Laboratory of the China University of Geosciences, Beijing, following the established methods (Liu *et al.*, 2014) modified from Maréchal *et al.* (1999). Briefly, at least 20 mg of sample powders were weighed in Teflon beakers based on their known Cu concentrations and then were digested in double-distilled HF + HNO_3 + HCl. After complete dissolution, the clear solutions were dried down at 80 °C. Subsequently, 1 ml of 8 N HCl + 0.001 % H_2O_2 was added to each beaker and the samples were heated to dryness again. This process was repeated three times and the final material was dissolved in 1 ml of 8 N HCl + 0.001 % H_2O_2. For the ion-exchange separation, each dissolved sample was loaded through a column containing pre-cleaned AG-MP-1M resin. Matrix elements were eluted in the first 10 ml of 8 N HCl + 0.001% H_2O_2, and Cu was collected in the following 24 ml of 8 N HCl + 0.001 % H_2O_2. The collected solutions were heated to dryness and re-dissolved in 3% HNO_3, which was repeated twice to remove all chlorine. Copper isotope analyses were carried out on a Thermo Scientific Neptune plus multi-collector inductively coupled mass spectrometer (MC-ICP-MS) instrument. Sample-standard bracketing method was used to correct for instrumental mass fractionation and drifting. For each measurement, data were collected over three blocks of 40 cycles with ~8 s integration.

Sulfide grains were separated from crushed rocks by conventional heavy liquid techniques and then were hand-picked under a binocular microscope. The copper isotope compositions of sulfide were measured at the State Key Laboratory for Mineral Deposits Research, Nanjing University. The detailed procedures were presented in Brzozowski *et al.* (2021). Briefly, about 1 mg of sulfide powders were successively digested in concentrated HNO_3 and 7 N HCl. After complete dissolution and repeated evaporation, the final material was dissolved in 1 ml of 7 N HCl. Purification of Cu was performed by ion-exchange chromatography using 0.2 ml of pre-cleaned AG MP-1 resin in a custom-made Teflon microcolumn. The 1 ml sample solution was loaded onto each column in one step and allowed sufficient time for the matrix elements to elute, leaving Cu, Fe, and Zn retained on the column. Then, the Cu was collected in the next 10 ml of 7 N HCl. After purification, the Cu solution was diluted to ~500 ppb in 2% HNO_3 and doped with 1 µg/g Ni (NIST SRM 986) for isotope measurement on a Thermo Scientific Neptune plus MC-ICP-MS using the sample-standard bracketing method. Nickel dopant was used as a monitor for mass bias. Each analysis consisted of 50 blocks of 4.2 s integrations. The reported $\delta^{65}Cu$ value for each sulfide grain is the average of two replicate analyses.

Sulfide melt inclusion compositions analysis

Major and trace element analyses for unexposed sulfide melt inclusions were conducted by LA-ICP-MS at the State Key Laboratory of Ore Deposit Geochemistry, IGCAS. Laser sampling was performed using an ASI RESOLution-LR-S155 laser microprobe equipped with a Coherent Compex-Pro 193 nm ArF excimer laser. An Agilent 7700x ICP-MS instrument was used to acquire ion-signal intensities. Helium (350 ml/min) was applied as a carrier gas. The ablated aerosol was mixed with Ar (900 ml/min) as a transport gas, before exiting the cell. In the process of the experiment, according to the diameter of the experimental object, the beam size slightly larger than its diameter is selected as far as possible, which can cover the whole range of the experimental object. The laser operating frequency is 5 Hz, the energy density of the sample surface is 5 J/cm^2, and the laser circle spot with a diameter of 26 ~ 80 μm is generated. Each analysis includes about 20 seconds of background acquisition. Data was then collected from the sample for 70 to 120 seconds.

Drilling the entire unexposed sulfide melt inclusion from the host mineral and subtracting the excess ablative host mineral from the resulting LA-ICP-MS signal know the constraints for matching the internal standard. STDGL3 was used to determine the concentrations of copper- and iron-philic elements, Fe and S were corrected as external standards, all other elements were corrected using NIST SRM 610, and the sum of S, Fe, Co, Ni and Cu was normalized to 100 %. Elements analysed include: ^{11}B, ^{23}Na, ^{25}Mg, ^{27}Al, ^{29}Si, ^{34}S, ^{57}Fe, ^{59}Co, ^{60}Ni, ^{65}Cu, ^{66}Zn, ^{71}Ga, ^{72}Ge, ^{75}As, ^{77}Se, ^{95}Mo, ^{107}Ag, ^{108}Pd, ^{109}Ag, ^{111}Cd, ^{115}In, ^{118}Sn, ^{121}Sb, ^{125}Te, ^{197}Au, ^{205}Tl, ^{208}Pb, ^{209}Bi (USGS reference principal element concentration values from the GeoReM database (http://georem.mpch-mainz.gwdg.de/)).

Numerical modelling

To understand the evolution trends of Cu concentration during continental and island arc magmatic differentiation, we ran quantitative models in which different types and proportions of magmatic sulfides crystallised in ideal equilibrium mode (Fig. 2d). We compiled a global dataset from GEOROC (http://georoc.mpch-mainz.gwdg.de/georoc/Entry.html) to obtain the major element contents (median values) of basalts to rhyolites at continental and island arcs. The corresponding Cu contents in global arc magmas were taken from Chiaradia (2014). The degree of crystallisation (F) and magma temperature were calculated using the correlations between silicate melt MgO content, based on the following equations:

$$X^{Total} = 0.01113319 \times (C_{MgO})^3 - 0.02301637 \times (C_{MgO})^2 - 9.35276623 \times (C_{MgO}) + 84.58 \quad \text{(Eq. S-2)}$$

$$T = -0.00220884 \times (X^{Total})^3 + 0.22166436 \times (X^{Total})^2 - 8.5164224 \times (X^{Total}) + 1164.34 \quad \text{(Eq. S-3)}$$

Where X^{Total} is the total magma crystallinity, C_{MgO} is the MgO content of the residual melt, T is the magma temperature in °C. These Equations are based on crystallisation experimental data of hydrous arc magmas (Chang and Audétat, 2018). We used the SCSS model of Smythe *et al.* (2017) to determine the S content of the silicate melt. In island arc magmas, due to the increase in S concentration in the residual silicate melts during magma differentiation under sulfide-undersaturated conditions, and the simultaneous decrease in S solubility caused by changes in melt composition and decreasing temperature, the magma inevitably reaches sulfide saturation when the MgO content in the residual melt drops to around 4.8 wt. %. In contrast, continental arc magmas reach sulfide saturation at the initial stages of differentiation. In these models, it is assumed that S precipitates only in the form of sulfides. The amounts of precipitated sulfides were calculated based on a sulfide S content of 38 wt. %. The amounts of Cu partitioning into minerals other than sulfides were neglected. The Cu partitioning between sulfide and silicate melt could be calculated using the above equations when the oxygen fugacity of the modelled magmas was fixed at ΔFMQ + 2.0 (Li and Audétat, 2015). The endmember case of ideal equilibrium crystallisation of sulfides was then modelled based on the equation:

$$C / C_0 = 1 / [1 + X / 100 (D^{Bulk} - 1)] \quad \text{(Eq. S-4)}$$

Where C is the Cu concentration in the residual melt, C_O is the Cu concentration in the original melt, X is the crystal fraction in wt. %, and D^{Bulk} is the bulk partition coefficient of Cu between the crystallised minerals and the residual melt. This equation corresponds to equations 4.17 in Rollinson (1993).

Supplementary Tables

Table S-1 Copper isotope and element analyses of the lower crustal cumulates and related sulfides from the Gangdese arc.

Sample number	SiO_2 (wt. %)	TiO_2 (wt. %)	Al_2O_3 (wt. %)	Fe_2O_3 (wt. %)	FeO (wt. %)	MnO (wt. %)	MgO (wt. %)	CaO (wt. %)	Na_2O (wt. %)	K_2O (wt. %)	P_2O_5 (wt. %)	S (wt. %)	$^{T}FeO^{*}$ (wt. %)	Cu (μg/g)	Type	$\delta^{65}Cu$ (‰)	2sd
Milin cumulate																	
ML19-3-19	42.13	1.64	13.52	4.21	7.11	0.13	14.45	11.20	2.40	0.43	0.01	0.25	10.90	218	whole-rock	0.07	0.03
ML19-3-71	42.01	1.90	13.94	3.10	8.17	0.16	14.25	10.85	2.64	0.62	0.01	0.01	10.96	202	whole-rock	-0.26	0.03
ML19-3-75	43.39	1.39	11.84	3.52	6.98	0.14	14.54	12.95	2.06	0.35	<0.01	0.11	10.15	547	whole-rock	0.07	0.02
ML19-3-78	42.65	1.88	12.24	2.97	7.43	0.13	14.60	12.90	2.07	0.48	<0.01	0.11	10.11	434	whole-rock	0.06	0.05
ML19-3-1	37.79	1.46	12.11	7.62	8.29	0.13	12.90	9.42	2.01	0.68	<0.01	4.00	15.14	4160	whole-rock	0.17	0.01
ML19-3-2	39.01	1.36	11.38	7.24	7.56	0.15	13.05	10.45	1.93	0.39	<0.01	4.33	14.07	8330	whole-rock	0.05	0.04
ML19-3-3	42.24	0.60	6.13	7.54	7.01	0.14	12.80	15.68	0.90	0.10	<0.01	4.70	13.79	7790	whole-rock	0.08	0.07
ML19-3-4	44.08	1.15	10.07	4.53	6.57	0.14	13.85	13.23	1.67	0.28	0.01	1.20	10.64	4340	whole-rock	-0.02	0.02
ML19-3-11	42.40	1.23	10.41	4.95	6.75	0.13	14.25	13.00	1.82	0.29	0.01	1.50	11.20	3800	whole-rock	0.12	0.07
Zhaxiraodeng cumulate																	
ML19-16-9	46.42	0.87	7.69	3.31	6.14	0.17	14.25	17.05	1.21	0.19	0.01	0.39	9.12	1045	whole-rock	0.13	0.02
ML19-4-28	36.50	1.18	11.92	11.25	9.79	0.20	9.84	8.93	1.67	0.49	0.04	7.10	19.91	>10000	whole-rock	-0.08	0.05
ML19-4-29	38.87	1.23	12.72	8.33	10.90	0.23	10.35	9.14	1.85	0.62	0.08	3.20	18.39	5760	whole-rock	-0.08	0.04
ML19-4-34	35.18	1.11	10.83	13.47	9.64	0.20	9.57	8.60	1.54	0.62	0.05	8.81	21.75	>10000	whole-rock	0.01	0.02
ML19-4-63	36.97	1.32	12.31	9.94	9.95	0.21	10.32	9.38	1.65	0.88	0.04	5.77	18.88	7530	whole-rock	0.00	0.00
ML19-15-13	38.61	1.23	12.41	8.62	9.67	0.20	10.35	9.62	1.78	0.64	0.02	4.50	17.42	4670	whole-rock	-0.03	0.04
ML19-15-14	41.16	1.36	13.01	6.20	9.43	0.24	11.85	9.84	1.89	0.64	0.04	1.50	15.00	2160	whole-rock	-0.12	0.05
ML19-6-3	42.87	0.95	13.67	6.00	8.88	0.19	10.85	10.35	1.97	0.64	0.09	1.08	14.27	1090	whole-rock	-0.09	0.02
Jinba Cumulate																	
ML19-1-38	44.43	1.27	19.30	3.87	8.63	0.17	5.74	10.30	3.24	0.50	0.43	0.05	12.11	134	whole-rock	0.51	0.03
ML19-1-43	39.52	2.69	10.04	8.83	10.50	0.31	11.15	10.60	1.41	0.40	0.91	0.86	18.44	673	whole-rock	-0.29	0.05
ML19-1-54	37.64	1.93	9.29	10.16	10.90	0.29	10.00	10.60	1.22	0.27	0.47	3.71	20.04	6010	whole-rock	-0.03	0.02
ML19-1-63	39.74	2.23	10.42	9.60	10.70	0.35	10.40	10.55	1.57	0.30	0.95	0.43	19.34	431	whole-rock	0.01	0.01
Cuijiu cumulate																	
JC17-2-1	42.69	1.01	19.17	5.86	6.32	0.18	6.08	12.31	2.42	0.59	0.38	0.02	11.59	82.9			
JC17-2-3	40.24	1.41	18.01	7.41	7.88	0.14	7.84	10.03	1.49	1.85	0.05	0.06	14.54	330	pyrite	-1.04	0.00
JC17-2-4	40.66	1.35	19.55	6.63	6.58	0.15	6.48	11.71	1.91	0.95	0.68	0.06	12.54	89.5			
JC17-2-7	43.17	1.22	19.13	4.31	6.20	0.16	7.19	11.73	2.01	0.89	0.60	0.01	10.07	95.6			
JC17-2-10	40.85	1.41	18.66	7.30	6.45	0.16	7.07	11.88	1.63	1.01	0.22	0.03	13.01	124			
JC17-2-11	40.63	1.37	17.35	7.55	7.12	0.17	7.41	11.88	1.68	1.04	0.44	0.04	13.91	154	pyrite	-0.93	0.04
JC17-2-13	38.68	1.77	14.83	10.05	8.65	0.18	8.95	10.81	1.68	0.98	0.30	0.04	17.68	246			

Sample number	SiO_2 (wt. %)	TiO_2 (wt. %)	Al_2O_3 (wt. %)	Fe_2O_3 (wt. %)	FeO (wt. %)	MnO (wt. %)	MgO (wt. %)	CaO (wt. %)	Na_2O (wt. %)	K_2O (wt. %)	P_2O_5 (wt. %)	S (wt. %)	$^{T}FeO^{*}$ (wt. %)	Cu (µg/g)	Type	$\delta^{65}Cu$ (‰)	2sd
JC17-2-15	39.75	1.28	18.70	8.15	6.55	0.16	6.39	12.61	1.55	1.06	0.60	0.02	13.88	129			
JC17-2-24	39.03	1.70	15.09	8.48	8.65	0.16	9.06	10.07	1.72	1.70	0.92	0.03	16.27	1005			
JC17-2-25	41.15	1.18	12.98	9.78	6.78	0.23	7.61	15.80	0.68	0.30	0.19	0.10	15.57	3429	chalcopyrite	-1.80	0.02
Sengbo cumulate																	
LZ18-32-7a	35.52	1.57	20.55	8.59	20.40	0.64	5.13	3.03	1.07	0.07	0.04	3.09	28.11	1470	chalcopyrite	-1.37	0.03
LZ18-32-7g	36.45	1.72	22.58	9.22	10.85	0.11	6.53	3.97	2.21	3.08	0.28	1.05	19.14	580	whole-rock	-2.09	0.02
LZ18-32-9a	41.17	1.22	24.93	8.49	6.94	0.05	4.77	3.26	3.30	2.68	0.04	3.12	14.57	2060	chalcopyrite	-1.57	0.03
LZ18-32-10a	34.25	1.79	20.45	7.87	22.70	0.60	4.66	3.08	1.14	0.08	0.04	4.20	29.76	2450	chalcopyrite	-1.78	0.02
LZ18-32-11a	35.78	1.45	23.86	10.26	11.25	0.13	6.16	3.17	2.09	3.03	0.10	0.58	20.49	392	whole-rock	-2.01	0.02
LZ18-32-15a	35.00	2.04	19.98	11.26	10.85	0.04	6.65	2.62	2.02	4.14	0.04	4.37	20.97	2760	chalcopyrite	-1.47	0.04
LZ18-34-15a	45.45	0.94	20.33	5.75	6.36	0.11	4.00	5.90	3.96	2.58	0.23	2.32	11.53	2610	whole-rock	-1.05	0.04
LZ18-34-6a	46.72	0.96	18.41	5.18	7.86	0.24	4.58	8.10	4.45	0.34	0.35	2.08	12.51	2280	whole-rock	-1.47	0.05
															sulfide	-0.42	0.01
LZ18-34-8-2a	44.86	1.39	21.38	7.06	7.37	0.09	4.00	6.36	3.84	2.22	0.16	0.08	13.72	65.9	sulfide	-0.29	0.03
LZ18-34-16a	48.41	1.09	22.04	4.19	5.18	0.09	2.44	8.63	4.68	0.59	0.48	0.14	8.95	172	sulfide	-0.68	0.00
LZ18-44-7a	46.02	0.88	17.86	5.24	6.13	0.21	5.22	12.20	3.24	0.61	0.29	0.88	10.84	152	sulfide	0.16	0.06
LZ18-44-23c	46.34	1.17	18.74	3.10	9.06	0.15	6.89	7.87	3.22	1.13	0.22	0.14	11.84	155	sulfide	-1.32	0.00
Milin meta-gabbro																	
LZ18-7-9-1a	44.63	2.20	20.22	3.16	8.90	0.17	4.37	10.65	3.09	0.63	0.77	0.14	11.74	26.9	sulfide	0.25	0.02
LZ18-7-9-2a	42.69	2.19	19.04	3.63	9.99	0.18	5.39	10.70	2.78	0.73	0.65	0.16	13.25	33.3	sulfide	0.15	0.03
LZ18-7-9-3a	43.24	2.22	19.52	3.78	9.28	0.14	5.04	10.55	2.98	0.76	0.63	0.27	12.67	59.1	sulfide	0.29	0.00
LZ18-7-9-4a	43.29	2.47	19.57	3.72	9.41	0.17	4.72	10.80	2.95	0.61	0.82	0.31	12.75	57.2	sulfide	0.29	0.03
LZ18-7-10a	42.23	2.37	19.28	4.17	8.84	0.15	4.55	11.05	2.86	0.61	0.77	0.49	12.58	67.0	sulfide	0.21	0.06
LZ18-7-13b	38.05	3.07	15.44	4.89	14.40	0.31	7.54	10.95	1.41	0.82	0.78	0.05	18.78	10.1	sulfide	0.12	0.04
LZ18-7-14a	42.83	2.53	19.23	4.26	9.51	0.11	4.87	8.83	2.72	1.97	0.82	0.72	13.34	162	sulfide	0.29	0.02
LZ18-7-15a	42.00	2.33	18.85	3.81	10.55	0.24	5.58	10.30	2.53	0.92	0.63	0.16	13.97	30.4	sulfide	0.29	0.04
LZ18-7-17a	40.76	2.62	17.98	3.61	12.95	0.45	6.01	10.15	1.88	0.95	0.75	0.03	16.18	6.60	sulfide	0.10	0.02

Table S-2 Composition of sulfide inclusions in the lower crustal cumulates from the Gangdese and other arcs.

Sample name	Size (μm)	S (wt. %)	Fe (wt. %)	Co (wt. %)	Ni (wt. %)	Cu (wt. %)	Data source
Lower crustal cumulates from Gangdese continental arc							
Milin							This study
ML19-3-19-2-2SI	26	55	38	0.7	3.6	3.5	
ML19-3-5-2-1SI	26	44	48	0.1	4.6	2.9	
ML19-3-19-1-1SI	26	51	38	0.4	1.8	8.2	
ML19-3-19-3-1SI	26	48	43	0.1	0.1	8.5	
zhaxiraodeng							
ML19-4-24-2-1SI	26	48	45	0.2	2.3	4.8	
ML19-4-24-4-1SI	26	43	53	0.1	1.8	2.9	
ML19-4-24-N1-1SI	26	42	56	0.2	0.2	2.3	
ML19-4-24-4-2SI	40	37	57	0.2	1.4	3.8	
ML19-15-14-2-1SI	26	39	40	0.2	1.4	19.4	
Cuijiu							
JC21-1-1(1)-2-5SI	26	30	45	0.0	0.0	25.3	
JC21-1-1(1)-2-4SI	26	30	40	0.4	0.0	29.1	
JC21-1-16-2-2SI	26	60	39	0.3	0.1	0.0	
Lilong							(Zhang *et al.*, 2022a)
19YS-1 SI2 hbl	35	40	52	0.2	1.4	6.7	
19YS-1 SI6 hbl	30	39	51	0.2	1.5	8.3	
19YS-2 SI3 hbl	20	38	55	0.3	0.9	5.2	
19YS-2 SI4 hbl	55	37	55	0.3	0.9	6.7	
19YS-2 SI6 hbl	20	38	54	0.3	1	6.1	
19YS-2 SI7 hbl	25	39	53	0.3	0.9	6.4	
19YS-2 SI9 hbl	20	38	54	0.3	1	6	
19YS-2 SI10 hbl	35	36	56	0.3	0.9	7.6	
19YS-2 SI11 hbl	35	36	57	0.3	1	5.9	
19YS-2 SI12 hbl	40	37	55	0.3	0.8	6.7	
19YS-4 SI2 hbl	30	38	58	0.2	0.4	3.5	
19SB-2 SI2 hbl	20	38	57	0.4	1.4	3.5	
19SB-2 SI3 hbl	60	36	55	0.3	1.2	7.7	
19SB-2 SI5 hbl	50	37	55	0.3	1.1	6.5	
19SB-2 SI6 hbl	90	34	58	0.3	1	6.4	
111HB SI1 SI11 hbl	30	39	60	0.2	0	1.3	
111HB SI2 hbl	35	39	60	0.2	0	1.2	
Laiyuan lower crustal cumulates from North China craton							
hornblendites							(Chang *et al.*, 2021)
YG11-8 ol SI	15	47	45	0.3	2.8	5.1	
YG11-1 bg hbl SI	20	43	53	0.2	2.2	2.2	
YG11-3 b hbl SI	50	37	52	0.3	2.6	7.6	
YG11-4 b hbl SI	70	39	51	0.3	3.1	7.2	
YG11-5 b hbl SI	25	39	56	0.2	1.9	3.2	
YG11-6 b hbl SI	60	37	55	0.2	1.9	5.1	
YG11-7 b hbl SI	45	41	52	0.2	2.2	4.3	
YG11-9 b hbl SI	30	42	53	0.1	1.6	3.7	
YG11-10 b hbl SI	20	39	55	0.2	2.3	4.1	
YG11-11 b hbl SI	28	42	51	0.3	2.7	4.3	

Sample name	Size (μm)	S (wt. %)	Fe (wt. %)	Co (wt. %)	Ni (wt. %)	Cu (wt. %)	Data source
YG6-1 b hbl SI	70	37	56	0.2	2.1	4.6	
YG6-2 b hbl SI	70	37	54	0.2	2.0	6.9	
YG6-3 b hbl SI	65	37	53	0.3	2.5	7.2	
YG6-4 b hbl SI	40	39	56	0.3	1.9	3.2	
YG6-5 brown hbl SI	50	38	56	0.2	1.6	4.7	
YG6-6 brown hbl SI	68	36	58	0.2	1.7	3.6	
YG6-8 opx SI1	30	43	49	0.2	2.0	5.1	
hornblendites							
LM7-1 opx SI1	60	40	55	0.4	4.1	0.9	
LM7-1 opx SI2	20	43	52	0.4	4.1	0.9	
LM7-7 opx SI	20	47	47	0.4	4.2	1.0	
LM7-8 brown hbl SI	40	41	54	0.3	3.2	1.1	
LM7-9 brown hbl SI1	55	38	57	0.3	3.4	1.0	
LM7-9 brown hbl SI2	25	40	55	0.3	3.5	1.0	
LM7-2 green hbl SI	30	41	53	0.5	4.3	0.8	
LM7-3 g-b hbl SI	20	40	54	0.5	4.6	0.8	
LM7-4 green hbl SI	30	42	54	0.3	2.8	1.0	
LM7-6 green hbl SI	32	40	54	0.4	4.2	0.8	
LM21-1 opx SI 70um	70	36	59	0.3	3.4	0.7	
LM21-6 opx SI 65um	65	38	56	0.2	2.3	3.9	
LM21-8 opx SI 35um	35	57	35	0.5	6.4	1.0	
LM21-9 opx SI 32um	32	40	55	0.3	3.8	0.8	(Chang *et al.*, 2021)
LM21-2 brown hbl SI	45	39	56	0.3	3.8	0.8	
LM21-3 brown hbl SI	48	35	60	0.3	3.5	1.1	
LM21-4 brown hbl SI	60	38	56	0.4	4.4	1.1	
LM21-5 b-g hbl SI	25	40	55	0.3	3.5	0.8	
LM21-7 green hbl SI	32	41	54	0.4	4.0	0.8	
pyroxenites							
LM27-4 brown hbl SI	48	36	54	0.7	6.6	2.0	
LM27-6 brown hbl SI	25	41	54	0.4	3.1	1.4	
LM27-8 brown hbl SI	25	41	54	0.4	2.9	1.4	
LM27-1 plag SI	30	43	52	0.3	4.6	0.6	
LM27-2 plag SI	40	39	54	0.4	5.8	1.4	
LM27-3 plag SI1	20	40	56	0.2	2.8	0.8	
LM27-3 plag SI2	15	39	56	0.5	3.7	1.1	
LM27-3 plag SI3	12	37	60	0.2	2.8	0.5	
LM27-5 plag SI	40	40	56	0.2	3.5	0.8	
LM27-9 plag SI	20	41	53	0.3	4.8	0.8	
LM34-2 opx SI	50	45	46	0.4	6.3	2.7	
LM34-3 hbl SI1	72	41	54	0.3	3.6	1.1	
LM34-3 hbl SI2	35	44	51	0.3	4.1	0.9	
LM34-3 hbl SI3	30	46	49	0.3	3.6	1.0	
LM34-1 plag SI	27	43	52	0.3	3.7	1.1	
Lower crustal cumulates from Kohistan island arc							
18JL015 SI2 hbl	20	36	49	0.5	3.8	10.4	
18JL016-1 expSI cpx	18	33	55	0.4	2	10.4	(Zhang *et al.*, 2022b)
18JL016-1 SI1 grt	16	41	44	0.5	2	12.3	

Sample name	Size (μm)	S (wt. %)	Fe (wt. %)	Co (wt. %)	Ni (wt. %)	Cu (wt. %)	Data source
18JL016-1 SI2 grt	14	34	54	0.4	1.5	10	(Zhang *et al.*, 2022b)
18JL016-1 SI3 grt	16	40	46	0.3	1.7	11.5	
18JL016-1 SI4 grt	16	31	60	0	0.3	8.9	
18JL016-2 SI1 grt	15	20	43	0.1	0.3	36.6	
18JL016-2 SI2 grt	25	32	47	0.3	1.5	19.3	
18JL016-2 SI3 grt	10	20	42	0	0.3	36.9	
18JL016-2 SI4 grt	10	17	45	0.1	0.2	37.3	
18JL016-2 SI6 grt	24	30	36	0.1	0.4	34.4	
18JL016-2 SI7 grt	14	25	30	0.1	0.4	45.4	
18JL016-2 SI8 grt	8	15	59	0.1	0.2	25.5	
18JL021 expSI1 grt	10	25	15	0	b.d.	59.5	
18JL021 expSI3 grt	40	24	21	0	0	55.1	
18JL029 SI1 hbl	15	34	57	0.3	0.4	8	
18JL029 SI2 hbl	12	32	60	0.3	0.4	6.7	
18JL029 SI3 hbl	30	42	49	0.3	0.3	7.6	
18JL029 SI4 hbl	35	39	49	0.3	0.3	11.2	

Supplementary Figures

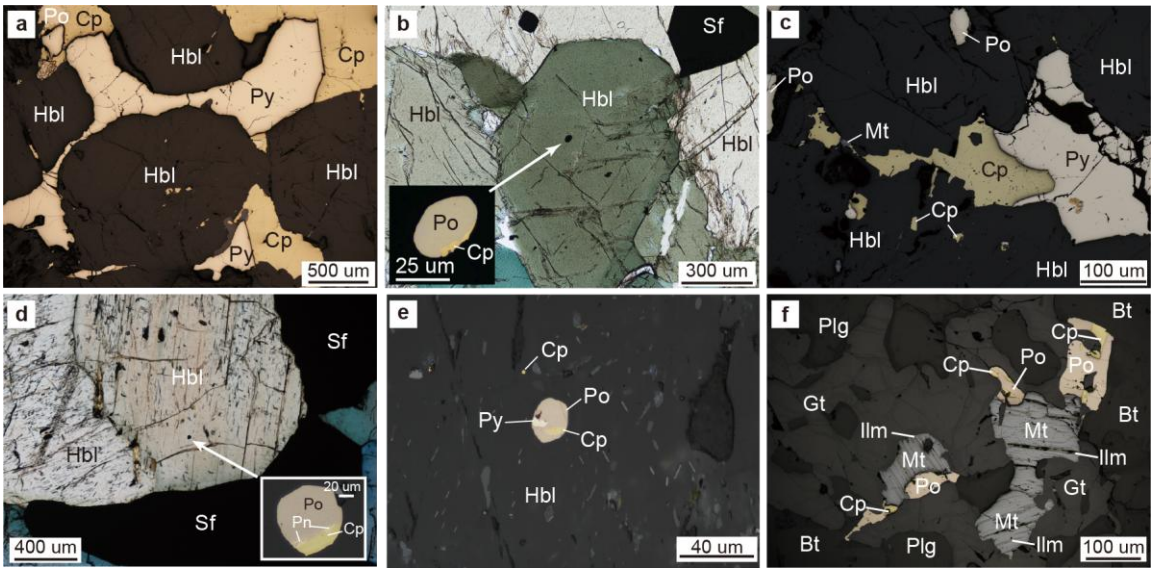

Figure S-1 Microphotographs of sulfides in the lower crustal cumulates from the Gangdese arc. **(a)** Milin cumulate: sulfides (Sf) infilling in the interstices between hornblende crystals (Hbl), consisting of pyrite (Py), pyrrhotite (Po) and chalcopyrite (Cp). **(b)** Milin cumulate: an exposed sulfide inclusion in hornblende. Sulfides consisting of pyrrhotite and chalcopyrite. **(c)** Zhaxiraodeng cumulate: sulfides infilling in the interstices between hornblende crystals. Sulfides consisting of pyrite, pyrrhotite and chalcopyrite. **(d)** Jinba cumulate: an exposed sulfide inclusion in hornblende. Sulfides consisting of pyrrhotite, chalcopyrite, and pentlandite (Pn). **(e)** Cuijiu cumulate: an exposed sulfide inclusion in hornblende. Sulfides consisting of pyrrhotite, chalcopyrite, and pyrite. **(f)** Sengbo cummulate: sulfides intergrowth with magnetite (Mt). Sulfides consisting of pyrrhotite and chalcopyrite. Bt = Biotite, Gt = Garnet, Ilm = Ilmenite.

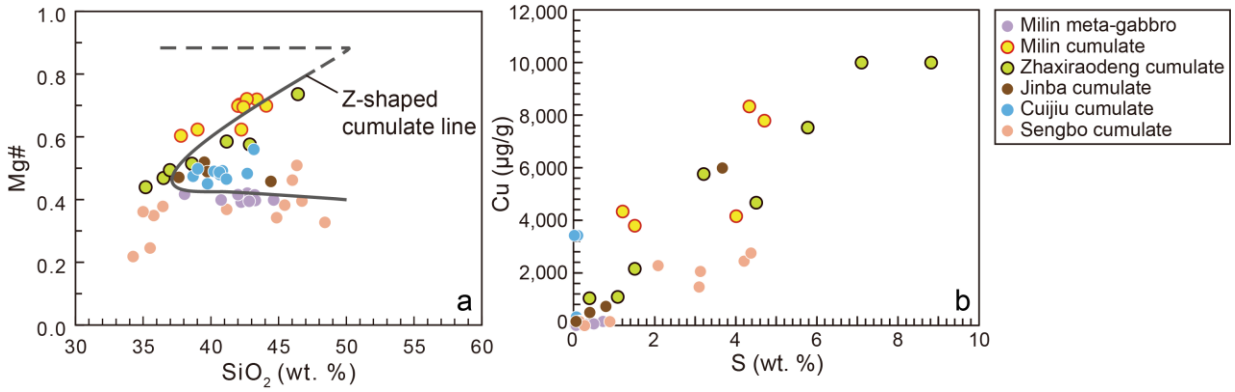

Figure S-2 Plot of whole-rock **(a)** SiO_2 versus Mg# and **(b)** Cu versus S contents for the lower crustal cumulates from the Gangdese arc.

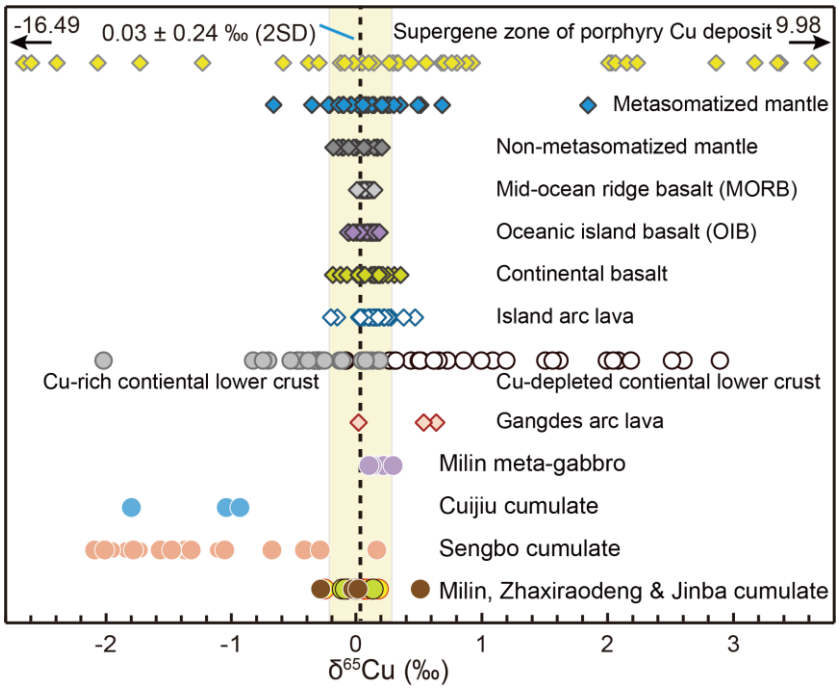

Figure S-3 $\delta^{65}Cu$ ranges of the Gangdese lower crustal cumulates. Vertical dashed line and yellow shaded bar represent the $\delta^{65}Cu$ range of depleted peridotites ($\delta^{65}Cu$ = 0.03‰ ± 0.24‰). Various geological reservoirs data (Mathur *et al.*, 2009; Liu *et al.*, 2015; Savage *et al.*, 2015; Moynier *et al.*, 2017; Wang *et al.*, 2019) are shown for comparison.

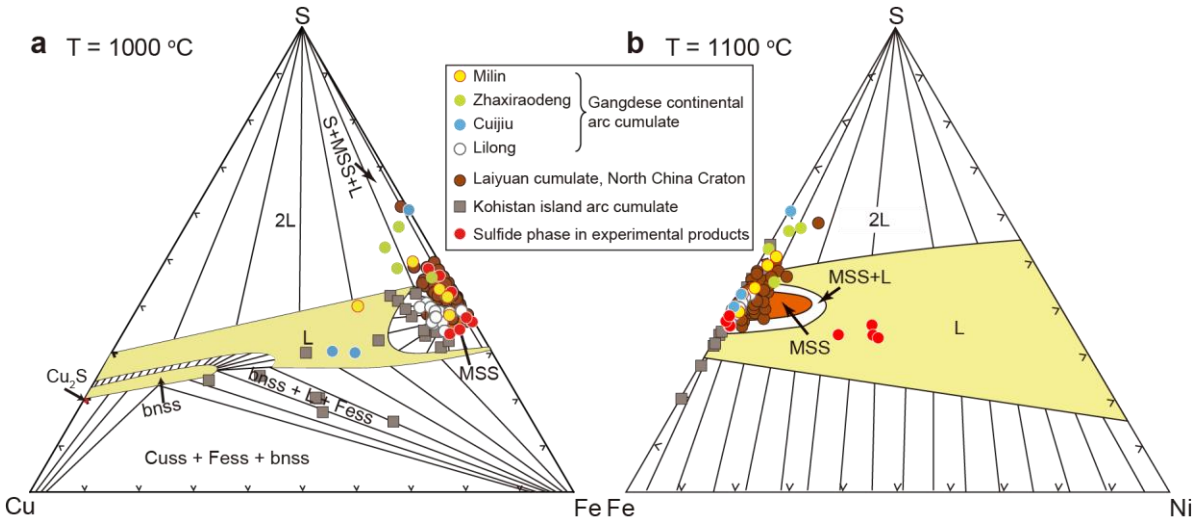

Figure S-4 Composition of magmatic sulfide inclusions projected onto the 1 bar Cu-Fe-S diagram at 1000 °C **(a)** and Fe-Ni-S diagram at 1100 °C **(b)** (Kullerud *et al.*, 1969). Data for Gangdese Lilong and Kohistan cumulates, and for Laiyuan cumulates are from Zhang *et al.* (2022a), Zhang *et al.* (2022b) and Chang *et al.* (2021), respectively. Sulfide phases in experimental products are from Xia *et al.* (2019). MSS = monosulfide solid solution.

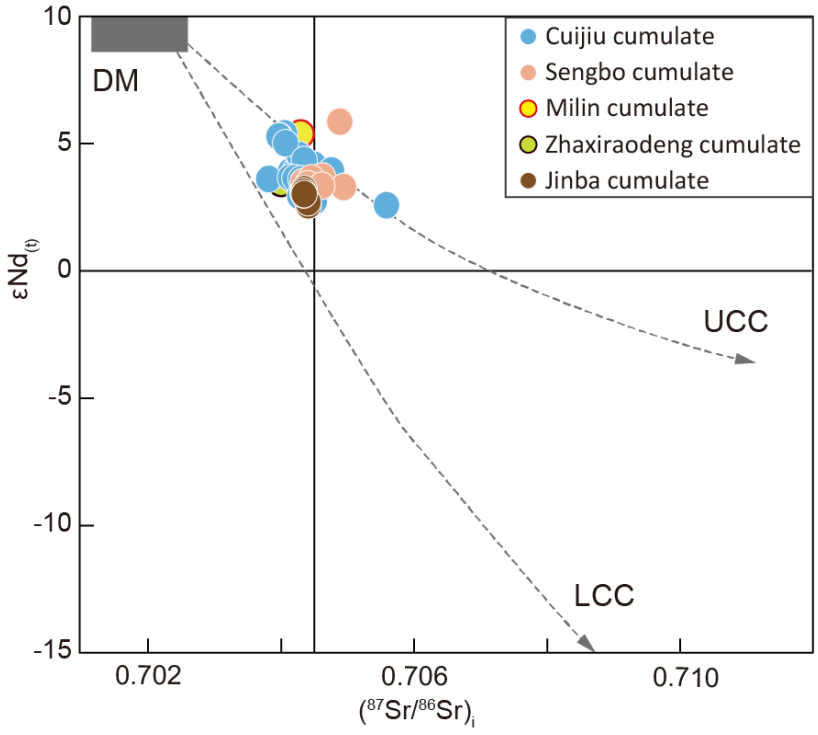

Figure S-5 Plot of whole-rock ($^{87}Sr/^{86}Sr$)i versus εNd(t) values for the lower crustal cumulates from the Gangdese arc. DM = Depleted mantle, LCC = lower continental crust, UCC = upper continental crust.

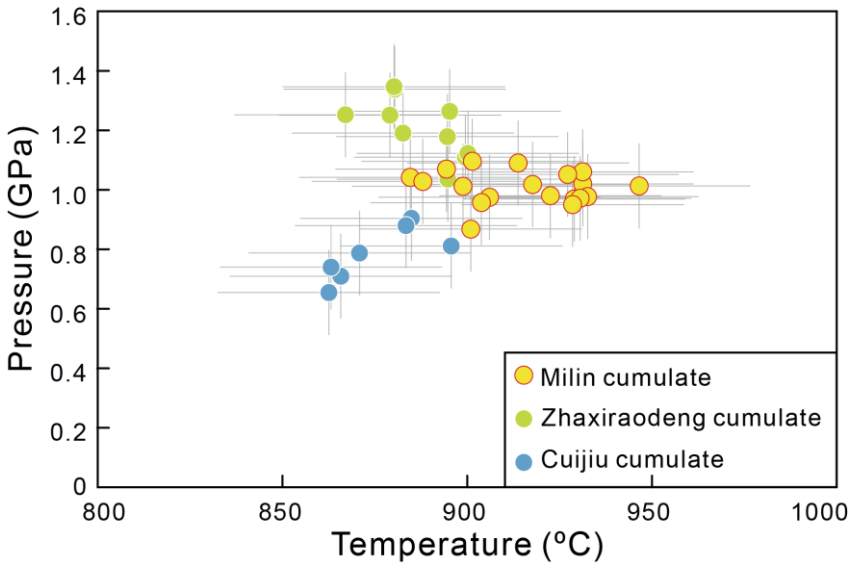

Figure S-6 Temperature and pressure results for the Gangdese cumulates. Temperature and pressure were estimated using the amphibole thermometer (equation 5) of Putirka (2016) and the amphibole barometer of Krawczynski *et al.* (2012), respectively.

Supplementary Information References

Brzozowski, M.J., Good, D.J., Wu, C., Li, W. (2021) Cu isotope systematics of conduit-type Cu–PGE mineralization in the Eastern Gabbro, Coldwell Complex, Canada. *Mineralium Deposita* 56, 707-724. http://doi.org/10.1007/s00126-020-00992-8

Chang, J., Audétat, A. (2018) Petrogenesis and Metal Content of Hornblende-Rich Xenoliths from Two Laramide-age Magma Systems in Southwestern USA: Insights into the Metal Budget of Arc Magmas. *Journal of Petrology* 59, 1869-1898. http://doi.org/10.1093/petrology/egy083

Chang, J., Audétat, A., Li, J.-W. (2021) Tectono-magmatic controls on decratonic gold deposits. *Contributions to Mineralogy and Petrology* 176, 69. http://doi.org/10.1007/s00410-021-01824-2

Chiaradia, M. (2014) Copper enrichment in arc magmas controlled by overriding plate thickness. *Nature Geoscience* 7, 43-46. http://doi.org/10.1038/ngeo2028

Krawczynski, M.J., Grove, T.L., Behrens, H. (2012) Amphibole stability in primitive arc magmas: effects of temperature, H2O content, and oxygen fugacity. *Contributions to Mineralogy and Petrology* 164, 317-339. http://doi.org/10.1007/s00410-012-0740-x

Kullerud, G., Yund, R.A., Moh, G.H. (1969) Phase Relations in the Cu-Fe-S, Cu-Ni-S, and Fe-Ni-S Systems. In: Wilson, H.D.B. (Ed.) *Magmatic Ore Deposits. Economic Geology Monograph Series 4.* Society of Economic Geologists. 323-343. https://doi.org/10.5382/Mono.04.23

Li, Y., Audétat, A. (2015) Effects of temperature, silicate melt composition, and oxygen fugacity on the partitioning of V, Mn, Co, Ni, Cu, Zn, As, Mo, Ag, Sn, Sb, W, Au, Pb, and Bi between sulfide phases and silicate melt. *Geochimica et Cosmochimica Acta* 162, 25-45. http://doi.org/10.1016/j.gca.2015.04.036

Liu, S.-A., Huang, J., Liu, J., Wörner, G., Yang, W., Tang, Y.-J., Chen, Y., Tang, L., Zheng, J., Li, S. (2015) Copper isotopic composition of the silicate Earth. *Earth and Planetary Science Letters* 427, 95-103. http://doi.org/10.1016/j.epsl.2015.06.061

Liu, S.-A., Teng, F.-Z., Li, S., Wei, G.-J., Ma, J.-L., Li, D. (2014) Copper and iron isotope fractionation during weathering and pedogenesis: Insights from saprolite profiles. *Geochimica et Cosmochimica Acta* 146, 59-75. http://doi.org/10.1016/j.gca.2014.09.040

Maréchal, C.N., Télouk, P., Albarède, F. (1999) Precise analysis of copper and zinc isotopic compositions by plasma-source mass spectrometry. *Chemical Geology* 156, 251-273. http://doi.org/10.1016/S0009-2541(98)00191-0

Mathur, R., Titley, S., Barra, F., Brantley, S., Wilson, M., Phillips, A., Munizaga, F., Maksaev, V., Vervoort, J., Hart, G. (2009) Exploration potential of Cu isotope fractionation in porphyry copper deposits. *Journal of Geochemical Exploration* 102, 1-6. http://doi.org/10.1016/j.gexplo.2008.09.004

Moynier, F., Vance, D., Fujii, T., Savage, P. (2017) The Isotope Geochemistry of Zinc and Copper. *Reviews in Mineralogy and Geochemistry* 82, 543-600. http://doi.org/10.2138/rmg.2017.82.13

Müntener, O., Ulmer, P. (2018) Arc crust formation and differentiation constrained by experimental petrology. *American Journal of Science* 318, 64-89. http://doi.org/10.2475/01.2018.04

Putirka, K. (2016) Amphibole thermometers and barometers for igneous systems and some implications for eruption mechanisms of felsic magmas at arc volcanoes. *American Mineralogist* 101, 841-858. http://doi.org/10.2138/am-2016-5506

Rollinson, H. (1993) Using geochemical data: evaluation, presentation, interpretation. Wiley, London.

Savage, P.S., Moynier, F., Chen, H., Shofner, G., Siebert, J., Badro, J., Puchtel, I.S. (2015) Copper isotope evidence for large-scale sulphide fractionation during Earth's differentiation. *Geochemical Perspectives Letters* 1, 53–64. http://doi.org/10.7185/geochemlet.1506

Smythe, D.J., Wood, B.J., Kiseeva, E.S. (2017) The S content of silicate melts at sulfide saturation: New experiments and a model incorporating the effects of sulfide composition. *American Mineralogist* 102, 795-803. http://doi.org/10.2138/am-2017-5800CCBY

Wang, Z., Park, J.-W., Wang, X., Zou, Z., Kim, J., Zhang, P., Li, M. (2019) Evolution of copper isotopes in arc systems: Insights from lavas and molten sulfur in Niuatahi volcano, Tonga rear arc. *Geochimica et Cosmochimica Acta* 250, 18-33. http://doi.org/10.1016/j.gca.2019.01.040

Xia, Y., Kiseeva, E.S., Wade, J., Huang, F. (2019) The effect of core segregation on the Cu and Zn isotope composition of the silicate Moon. *Geochemical Perspectives Letters* 12, 12-17. http://doi.org/10.7185/geochemlet.1928

Xu, W., Zhu, D.-C., Wang, Q., Weinberg, R.F., Wang, R., Li, S.-M., Zhang, L.-L., Zhao, Z.-D. (2019) Constructing the Early Mesozoic Gangdese Crust in Southern Tibet by Hornblende-dominated Magmatic Differentiation. *Journal of Petrology* 60, 515-552. http://doi.org/10.1093/petrology/egz005

Zhang, J., Chang, J., Wang, R., Audétat, A. (2022a) Can Post-Subduction Porphyry Cu Magmas Form by Partial Melting of Typical Lower Crustal Amphibole-Rich Cumulates? Petrographic and Experimental Constraints from Samples of the Kohistan and Gangdese Arc Roots. *Journal of Petrology* 63, egac101. http://doi.org/10.1093/petrology/egac101

Zhang, J., Wang, R., Hong, J. (2022b) Amphibole fractionation and its potential redox effect on arc crust: Evidence from the Kohistan arc cumulates. *American Mineralogist* 107, 1779-1788. http://doi.org/10.2138/am-2022-8141

Zhang, Z., Ding, H., Palin, R.M., Dong, X., Tian, Z., Chen, Y. (2020) The lower crust of the Gangdese magmatic arc, southern Tibet, implication for the growth of continental crust. *Gondwana Research* 77, 136-146. http://doi.org/10.1016/j.gr.2019.07.010